CHEMISTRY OF MATERIALS
Article
pubs.acs.org/cm

$LiCe(BH_4)_3Cl$, a New Lithium-Ion Conductor and Hydrogen Storage Material with Isolated Tetranuclear Anionic Clusters

Morten B. Ley,[†,∥] Dorthe B. Ravnsbæk,[†,∥,∇] Yaroslav Filinchuk,*[,‡] Young-Su Lee,[§] Raphaël Janot,[⊥] Young Whan Cho,[§] Jørgen Skibsted,[#,∥] and Torben R. Jensen*[,†,∥]

[†]Center for Materials Crystallography (*CMC*), Interdisciplinary Nanoscience Center (*iNANO*), [#]Instrument Centre for Solid-State NMR Spectroscopy, Interdisciplinary Nanoscience Center (*iNANO*), and [∥]Department of Chemistry, Aarhus University, Langelandsgade 140, DK-8000 Aarhus C, Denmark

[‡]Institute of Condensed Matter and Nanosciences, Université Catholique de Louvain, Place L. Pasteur 1, B-1348, Louvain-la-Neuve, Belgium

[§]High Temperature Energy Materials Research Center, Korea Institute of Science and Technology, Seoul 136-791, Republic of Korea

[⊥]Laboratoire de Réactivité et Chimie des Solides, UMR 6007 CNRS, Université de Picardie - Jules Verne, Amiens Cedex, France

S *Supporting Information*

ABSTRACT: Mechanochemical synthesis using $CeCl_3$-MBH_4 (M = Li, Na or K) mixtures are investigated and produced a new compound, $LiCe(BH_4)_3Cl$, which crystallizes in a cubic space group $I\bar{4}3m$, $a = 11.7204(2)$ Å. The structure contains isolated tetranuclear anionic clusters $[Ce_4Cl_4(BH_4)_{12}]^{4-}$ with a distorted cubane Ce_4Cl_4 core, charge-balanced by Li^+ cations. Each Ce atom coordinates three chloride ions and three borohydride groups via the η^3−BH_3 faces, thus completing the coordination environment to an octahedron. Combination of synchrotron radiation powder X-ray diffraction (SR-PXD), powder neutron diffraction and density functional theory (DFT) optimization show that Li cations are disordered, occupying 2/3 of the 12*d* Wyckoff site. DFT calculation indicates that $LiCe(BH_4)_3Cl$ is stabilized by higher entropy rather than lower enthalpy, in accord with the disorder in Li positions. The structural model also agrees well with the very high lithium ion conductivity measured for $LiCe(BH_4)_3Cl$ of 1×10^{-4} Scm^{-1} at $T = 20$ °C. In situ SR-PXD reveals that the decomposition products consist of LiCl, CeB_6 and CeH_2. The Sieverts measurements show that 4.7 wt % H_2 is released during heating to 500 °C. After rehydrogenation at 400 °C and $p(H_2) = 100$ bar for 24 h an amount of 1.8 wt % H_2 is released in the second dehydrogenation. The ^{11}B MAS NMR spectra of the central and satellite transitions for $LiCe(B(D/H)_4)_3Cl$ reveal highly asymmetric manifolds of spinning sidebands from a single ^{11}B site, reflecting dipolar couplings of the ^{11}B nuclear spin with the paramagnetic electron spin of the Ce^{3+} ions.

KEYWORDS: *lithium ion conductor, hydrogen storage, borohydride, powder X-ray diffraction, reversibility*

■ INTRODUCTION

The transition toward a sustainable, environmentally friendly and carbon free energy system that can fulfill the increasing energy demands is considered one of the greatest challenges in the 21st century.[1] In particular, a safe, compact, and efficient means of storage of renewable energy still remains to be identified. Chemical storage of energy as hydrogen or electricity in a battery is among the most promising approaches with a potential to reach the required high energy contents.[2−4] This has prompted the present research project where a new lithium- and cerium -based borohydride chloride is prepared and characterized.

Hydrogen is abundant, easy to produce by electrolysis, and has the potential to be stored efficiently in the solid state, e.g,. as metal borohydrides, which currently receive increasing interest. Unfortunately, many of the known borohydrides exhibit poor thermodynamic and kinetic properties, which hamper their utilization in technological applications.[5−8] Therefore, significant focus has been on synthesis and characterization of novel bimetallic borohydrides because of their somewhat tunable decomposition temperatures.[9−12] Furthermore, recent studies of metal borohydrides reveal a remarkable diversity in the structural topologies illustrated by a new nanoporous magnesium borohydride γ-$Mg(BH_4)_2$ with 33% empty volume.[13] The compounds $LiZn_2(BH_4)_5$ and $NaZn_2(BH_4)_5$ are built from two identical interpenetrated three-dimensional frameworks consisting of isolated complex anions, $[Zn_2(BH_4)_5]^-$, whereas $NaZn(BH_4)_3$ consists of isolated anions of $[Zn(BH_4)_3]^-$ counter balanced by sodium.[14,15] Isolated complex anions have also been observed in other structures, such as $[Sc(BH_4)_4]^-$ in $MSc(BH_4)_4$ (M = Li, Na or K) or $[Zn(BH_4)Cl_2]^-$ in the heteroleptic borohydride, $KZn(BH_4)Cl_2$.[16−20] Several of these mixed-metal borohydrides exhibit improved thermodynamic and kinetic properties, e.g. $LiSc(BH_4)_4$ and $NaSc(BH_4)_4$ are found to decompose in the temperature ranges 140 to 260 °C and 167 to 267 °C, respectively.[16−18] These are significantly lower temperatures as compared to the corresponding alkali borohydrides, $LiBH_4$ and $NaBH_4$, which decompose at approximately 380 and 400 °C, respectively.[21]

The complex borohydride ion may resemble the halide ions in the solid state, which may facilitate anion substitution in metal borohydrides. The halide stabilized lithium borohydride

Received: March 12, 2012
Published: April 9, 2012

ACS Publications

$LiBH_4$−LiX, X═Cl, Br, I, form solid solutions, $Li(BH_4)_{1-x}X_x$, which tend to stabilize the hexagonal polymorph to room temperature.[22−24] The hexagonal halide stabilized polymorphs h-$Li(BH_4)_{1-x}X_x$, were found to have very high lithium ion conductivities in the range 1×10^{-5} to 1×10^{-4} Scm^{-1} at room temperature, RT, which increase to about 1×10^{-2} S cm^{-1} at 150 °C.[25] These materials are considered as possible electrolytes for solid-state lithium batteries.[26]

Structural, thermodynamic and kinetic properties as well as thermal stability and decomposition reactions are of vital importance for possible applications of reversible hydrogen carriers and rechargeable lithium battery materials. In some cases, metal borohydrides may release gaseous boranes, such as diborane, which leads to decreasing storage capacity of the hydrogen storage system.[27] Therefore, formation of metal borides during decomposition is an important indication of possible reversibility, since boron is kept in the solid state. Furthermore, formation of metal borides is preferred to formation of elemental boron due to the high stability of the latter. Therefore, detailed characterization of new lithium containing metal borohydrides may open new routes for design and preparation of materials with a potential utilization for hydrogen storage or lithium batteries.

Here we report on the synthesis, characterization and thermal decomposition of a new lithium borohydride material, $LiCe(BH_4)_3Cl$ by in situ synchrotron radiation powder X-ray diffraction (SR-PXD), powder neutron diffraction (PND), density functional theory (DFT) optimizations, solid-state magic angle spinning (MAS) nuclear magnetic resonance (NMR), thermal analysis and Sievert measurements.

EXPERIMENTAL SECTION

Synthesis. The title compound was prepared from samples of $CeCl_3$−$LiBH_4$ in the molar ratios 1:2, 1:3, and 1:4, denoted samples **s1**−**s3**, **s5** respectively (see Table 1). The samples were ball-milled (BM) in repeated sequences of 2 min BM and 2 min pauses for 60 repetitions using a Fritsch Pulverisette 4 planetary mill under inert conditions (argon atmosphere) in 80 mL of tungsten carbide steel containers with tungsten carbide balls (o.d. Ten mm). The sample to balls mass ratio was approximately 1:35. Speeds of the main disk and of the planetary disks were 200 and 560 rpm, respectively.

Table 1. Composition of the Investigated Samples and Synthesis Products Obtained after Mechanochemical Treatment As Observed by PXD (M═Li, Na or K)

sample	reactants	ratio	mole fraction x(MBH_4)	synthesis products
s1	$CeCl_3$−$LiBH_4$	1:2	0.672	$LiCe(BH_4)_3Cl$, LiCl
s2	$CeCl_3$−$LiBH_4$	1:3	0.750	$LiCe(BH_4)_3Cl$, LiCl
s3	$CeCl_3$−$LiBH_4$	1:4	0.800	$LiCe(BH_4)_3Cl$, LiCl
s4	$CeCl_3$−$Li^{11}BD_4$	1:3	0.755	$LiCe(^{11}BD_4)_3Cl$, LiCl
s5	$CeCl_3$−$LiBH_4$	1:3	0.754	$LiCe(BH_4)_3Cl$, LiCl
s6	$CeCl_3$−$NaBH_4$	1:3	0.749	$CeCl_3$, $NaBH_4$
s7	$CeCl_3$−$NaBH_4$	1:4	0.799	$CeCl_3$, $NaBH_4$
s8	$CeCl_3$−KBH_4	1:3	0.756	$CeCl_3$, KBH_4
s9	$CeCl_3$−KBH_4	1:4	0.807	$CeCl_3$, KBH_4

A sample for neutron diffraction experiments was prepared from $CeCl_3$−$Li^{11}BD_4$ in molar ratio 1:3 (sample **s4**) using the same milling conditions as described above. Furthermore, samples of $CeCl_3$-MBH_4 (M═Na or K) in molar ratios 1:3 and 1:4 (samples **s6**−**s9**, respectively) were prepared by ball milling. The $CeCl_3$−KBH_4 samples (**s8** and **s9**) were subjected to the same ball milling conditions as used for sample **s1**−**s5**. The $CeCl_3$−$NaBH_4$ samples (**s6** and **s7**) were also initially ball milled using these conditions, however, as no reaction occurred, the samples were subsequently ball milled for additional 30 repetitions applying 2 min BM and 2 min pauses with speeds of the main disk and the planetary disks of 250 and 625 rpm, respectively.

All preparation and manipulation of the samples were performed in a glovebox with a circulation purifier maintained under an argon atmosphere with <1 ppm of O_2 and H_2O. The chemicals used were anhydrous cerium chloride, $CeCl_3$ (Sigma-Aldrich 99.9%), lithium borohydride, $LiBH_4$ (Sigma-Aldrich, 95%), lithium borodeuteride, $Li^{11}BD_4$ (KatChem, 95%), sodium borohydride (Sigma-Aldrich, 95%) and potassium borohydride (Sigma-Aldrich, 95%). All chemicals were used as received.

Laboratory Powder X-ray Diffraction. All samples were initially investigated using laboratory powder X-ray diffraction (PXD) in order to identify the reaction products and estimate the crystallinity of the samples. PXD measurements were performed in Debye−Scherrer transmission geometry using a Stoe diffractometer equipped with a curved Ge(111) monochromator (Cu Kα_1 radiation, λ = 1.54060 Å) and a curved position sensitive detector. Data were collected at RT from 4 to 127° 2θ with counting times of ~960 s per step. Air-sensitive samples were mounted in a glovebox in 0.5 mm glass capillaries sealed with glue.

In situ Synchrotron Radiation Powder X-ray Diffraction. In situ SR-PXD data was collected at the Swiss-Norwegian Beamlines (SNBL) at the European Synchrotron Radiation Facility (ESRF) in Grenoble, France. A glass capillary (o.d. 0.5 mm) containing the sample was heated from RT to 500 °C at a rate of 8 °C/min, while SR-PXD data was collected. The temperature was controlled with a Cyberstar hot air blower. The data were collected using a MAR345 image plate detector at a sample to detector distance of 250 mm, and a selected X-ray wavelength of λ = 0.709637 Å. The capillary was oscillated 30° during X-ray exposure of the sample for 30 s.

All obtained raw images were transformed to powder patterns using the FIT2D program,[28] which was also used for calibration of the X-ray wavelength and the sample−detector distance using a SR-PXD measurements of the standard NIST LaB_6 and masking diffraction spots from the single-crystal sapphire sample holder. Uncertainties of the integrated intensities were calculated at each 2θ point by applying Poisson statistics to the intensity data, considering the geometry of the detector.[29]

Powder Neutron Diffraction. The powder neutron diffraction (PND) experiment was conducted at the high-resolution powder neutron diffractometer HRPT at the spallation neutron source SINQ at Paul Scherrer Institute in Villigen, Switzerland.[30] The powder sample of ball milled $CeCl_3$−$Li^{11}BD_4$ (1:3, **s4**) was enclosed in a vanadium can (8 mm diameter), and data was collected with a neutron wavelength of λ = 1.494 Å in the high intensity mode using the standard ILL-type Orange cryostat at −271, −248, −223, and 25 °C.

Structure Solution of $LiCe(BH_4)_3Cl$. SR-PXD data collected at ~160 °C for $CeCl_3$−$LiBH_4$ (1:4, **s4**), containing the highest fraction of the new compound, was used for indexing and structure solution. Indexing of the diffraction peaks was performed using the program Dicvol in a body centered cubic cell (a = 11.7204(2) Å).[31] The structure was solved in space group $I\bar{4}3m$ by global optimization in direct space using the program FOX,[32] using one Ce, one Li, and one Cl atom, and a rigid tetrahedral BH_4 group as optimized units and a number of antibump restraints. The structure contains one cerium and one chloride atom located on 8c Wyckoff sites, while boron is located on the 24g Wyckoff site. The crystallographic positions of Ce, B, and Cl determined from PXD and PND, respectively, are similar. However, SR-PXD data alone showed some ambiguity for the Li positions. Therefore, the position was determined from the combination of SR-PXD data, PND data and DFT optimization of the resulting models (discussed in more detail below). The only Li position consistent with all diffraction data and energy minimizations is the 12d Wyckoff site. The Li occupancy refines to ca. 2/3, corresponding to the expected 8 Li atoms per unit cell. A symmetry check in Platon[33] did not suggest higher metric or crystallographic symmetry. According to the multiplicity $Z = 8$, the crystallographic density for the $LiCe(BH_4)_3Cl$ compound is $\rho = 1.87$ g cm^{-3}.

The final Rietveld refinement was performed using the PND data measured at −248 °C on $CeCl_3$–$Li^{11}BD_4$ (1:3, **s4**) and subsequently the SR-PXD data measured at ~160 °C on $CeCl_3$–$LiBH_4$ (1:4, **s3**) using the program Fullprof,[34] see Figure 1a and 1b. The background was described by linear interpolation between selected points. Due to an artifact SR-PXD data region 18.7–19.5° 2θ was omitted in the refinement. The final refinement on the SR-PXD data resulted in the following refinement factors, $R_B = 2.52\%$, $R_F = 1.6\%$, $R_p = 2.62\%$, $R_{wp} = 3.32\%$ (not corrected for background) and $R_p = 5.1\%$, $R_{wp} = 5.98\%$ (corrected for background) and $\chi^2 = 3760$ (this value is high due to the very high counting statistics accumulated by the 2D detector). The refinement factors from the PND data are $R_B = 5.50\%$, $R_F = 2.90\%$, $R_p = 2.67\%$, $R_{wp} = 3.55\%$ (not corrected for background) and $R_p = 9.43\%$, $R_{wp} = 10.4\%$ (corrected for background) and $\chi^2 = 3084$. The unit-cell parameter refines to $a = 11.4993(4)$ Å using the PND data. The strongest reflections has a less strong influence in the Rietveld refinements due to the used weighting scheme: $1/\sigma(I) = 1/(I)^{1/2}$. However, the relative error is expected in average to be the same as for other peaks. There was no indication of any preferred orientation in the cubic structure. The atomic coordinates for $LiCe(BH_4)_3Cl$ as found from the final refinement on SR-PXD and PND data are shown in Tables S1 and S2 in the Supporting Information.

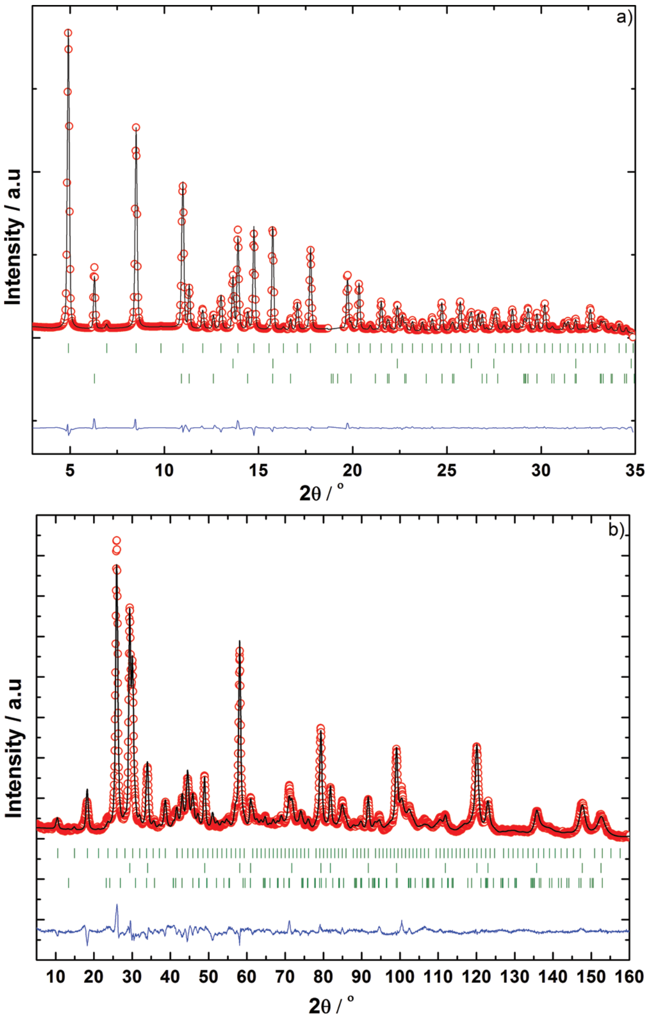

Figure 1. Rietveld refinement profile of (a) SR-PXD data for $CeCl_3$–$LiBH_4$ (1:4, s3) measured at ~160 °C and (b) PND data measured at −248 °C of $CeCl_3$–$Li^{11}BD_4$ (1:3, s4) The samples both contain the novel phase $LiCe(BH_4)_3Cl$ (top), unreacted $CeCl_3$ (bottom), and LiCl (middle). An artifact between 2θ values of 18.7 and 19.5° was omitted in the refinement of the SR-PXD data. SR-PXD data obtained at BM01A, ESRF, Grenoble, France, $\lambda = 0.709637$ Å, PND data obtained at SINQ at PSI in Villigen, Switzerland, $\lambda = 1.494$ Å.

First-Principles Calculations. Several candidate structures derived from the PXD and PND data were examined by density functional theory calculations. The calculations were performed within the generalized-gradient approximation by Perdew, Burke, and Ernzerhof[35] as implemented in the Vienna Ab-initio Simulation Package.[36] Projector augmented wave (PAW) potential with a planewave cutoff energy of 600 eV is used.[37] For each atomic species, Li, Ce, B, H, and Cl, the PAW potentials Li_sv, Ce_3, B, H, and Cl are used, respectively. Three valence electrons are included in the Li_sv potential, and a 4f electron in Ce is frozen to core in the Ce_3 potential.

A primitive cell having four formula units of $LiCe(BH_4)_3Cl$ is used. Regular k-point meshes of 2 × 2 × 2 in the first Brillouin zone including is Γ point are sampled, which ensures energy convergence within 0.2 meV/f.u. Structural optimization was performed until the force on each atom became smaller than 0.005 eV/Å. During the optimization the lattice parameter was fixed to the experimental value from the SR-PXD analysis. Partial occupation at the 12d or 24g (discussed in detail below) sites is modeled in the DFT optimization by removing the 3-fold axes along the ⟨111⟩ directions, which reduces the symmetry to the space group $I\bar{4}2m$ (see Figure S1a in the Supporting Information for the 12d model). The final atomic coordinates from the DFT optimization in the I-43m space group was derived by applying 3-fold rotation along ⟨111⟩ to the 12d model (discussed in detail below).

Solid-State ^{11}B MAS NMR Spectroscopy. Solid-state ^{11}B MAS NMR spectra were obtained on Varian INOVA-400 (9.4 T) and Varian Direct-Drive VNMRS-600 (14.1 T) spectrometers using home-built X-{^{1}H} CP/MAS NMR probes for 5 mm and 4 mm o.d. rotors, respectively. The experiments used ^{11}B rf field strengths of $\gamma B_1/2\pi$ = 52 kHz (9.4 T) and $\gamma B_1/2\pi$ = 60 kHz (14.1 T), a 4 s relaxation delay, and ^{1}H decoupling during acquisition ($\gamma B_2/2\pi \approx 45$ kHz at both magnetic fields). The NMR experiments were performed at ambient temperature using airtight, end-capped zirconia rotors packed with the samples in a Ar-filled glovebox. The ^{11}B isotropic chemical shifts are in ppm relative to $F_3B{\cdot}O(CH_2CH_3)_2$.

Conductivity Measurements. Electrochemical Impedance Spectroscopy (EIS) measurements were performed using a BioLogic VMP3 potentiostat. Either steel disks (ion blocking) or lithium foils (nonblocking) were used as electrodes. Impedance (a.c.) spectra were recorded at RT between 1 MHz and 10 mHz, with a voltage perturbation of 25 mV. From the Nyquist plots of the complex impedance (imaginary part Z_{im} as a function of the real part Z_{re}), the resistances of the samples were obtained from the diameter of the semicircle and from the intercept on the Z_{re} axis for $LiBH_4$ (reference sample) and $LiCe(BH_4)_3Cl$, respectively. The conductivity measurements were performed on five pellets made from sample $CeCl_3$–$LiBH_4$ (1:3, **s5**). The pellets with a diameter of 10 mm and with thicknesses in the range 0.5 to 2.0 mm were prepared by using a uniaxial press (900 MPa). Sintering of the pellets was performed at RT due to possible decomposition of the materials at elevated temperatures. The pellets densities were ca. 2.42 g cm^{-3}, which corresponds to a compactness of 93%, calculated using the density of sample $CeCl_3$–$LiBH_4$ (1:3, **s5**) derived from the Rietveld refined composition, ρ(**s5**) = 2.61 g cm^{-3}.

Thermal Analysis and Sievert Measurements. The samples $CeCl_3$–$LiBH_4$ (1:3, **s2**) and (1:4, **s3**) were studied by thermogravimetric analysis (TGA), differential scanning calorimetry (DSC) and Sieverts' measurements. Simultaneous TGA and DSC were performed using a Netzsch STA449C Jupiter instrument in the temperature range RT to 500 °C ($\Delta T/\Delta t$ = 10 °C/min) using corundum crucibles with lid as sample holder. The experiments were conducted in helium (4.6) atmosphere.

The cyclic reversibility of hydrogen release and uptake was studied by Sieverts' measurements using a PCTPro 2000 apparatus.[38,39] Three desorption and two absorption cycles were measured for ca. 150 mg of material. Hydrogen desorption data was collected during heating from RT to 500 °C ($\Delta T/\Delta t = 1$ °C/min) and then keeping the temperature constant at 500 °C for 3 h with a back pressure of $p(H_2) = 1$ bar. Hydrogen absorption measurements was performed before the second and third desorption cycle at 400 °C and $p(H_2) = 100$ bar for 24 h.

■ RESULTS AND DISCUSSION

Synthesis and Initial Phase Analysis. Lithium cerium borohydride chloride, $LiCe(BH_4)_3Cl$ was synthesized by a mechano-chemistry, i.e. ball milling (BM) of samples $CeCl_3$−$LiBH_4$ (1:3, **s2**) and (1:4, **s3**). The SR-PXD data, collected at RT after BM, show diffraction peaks from $LiCe(BH_4)_3Cl$, LiCl, and $CeCl_3$, indicating that the reaction shown in (**1**) occurs.

$$CeCl_3 + 3LiBH_4 \rightarrow LiCe(BH_4)_3Cl + 2LiCl \quad (1)$$

The gravimetric and volumetric hydrogen density for $LiCe(BH_4)_3Cl$ is $\rho_m = 5.37$ wt % H_2 and $\rho_v = 99.8$ kg H_2/m^3, respectively. The reaction between $CeCl_3$ and $LiBH_4$ is a complex reaction, which is believed to be a coupled metathesis and addition reaction leading to the formation of $LiCe(BH_4)_3Cl$ and LiCl. The optimal stoichiometry between reactants according to reaction 1 is 1:3. However, the reaction is not completed using the selected ball milling conditions, as unreacted $CeCl_3$ is identified by PXD.

Upon heating, the reaction between $CeCl_3$ and $LiBH_4$ continues from 100 to 160 °C, where the maximum amount of $LiCe(BH_4)_3Cl$ is observed by SR-PXD. The composition of **s3** at 160 °C found by Rietveld refinement is $LiCe(BH_4)_3Cl$ 62 wt % (32 mol %), LiCl 22 wt % (61 mol %), and $CeCl_3$ 16 wt % (7 mol %). **s4** used for the PND experiment and ^{11}B MAS NMR analysis was also analyzed with SR-PXD measured at RT, and the overall sample composition was $LiCe(^{11}BD_4)_3Cl$ 66 wt % (28 mol %), LiCl 29 wt % (70 mol %) and $CeCl_3$ 5 wt % (2 mol %), which indicates that reaction 1 has occurred to a higher extent during BM for this sample. Crystalline lithium borohydride is not observed in the synthesis products for any of the samples by SR-PXD or PND. However, $LiBH_4$ was confirmed to be present in an amorphous state by NMR analysis (see below). Prolonged ball milling times or conditions facilitating higher energy during ball milling are possibly needed to complete reaction 1.[40] The samples $CeCl_3$−$NaBH_4$ and $CeCl_3$−KBH_4 were treated at similar mechano-chemical conditions as compared to the $CeCl_3$−$LiBH_4$ samples but no indications for chemical reaction were observed.

Crystal Structure of $LiCe(BH_4)_3Cl$. $LiCe(BH_4)_3Cl$ crystallizes in a cubic unit cell, $a = 11.7204(2)$ Å, with space group symmetry $I\bar{4}3m$ (see Figure 2). The positions of Ce, B and Cl ions were readily determined from the SR-PXD data. The structure contains isolated tetranuclear anionic clusters of $[Ce_4Cl_4(BH_4)_{12}]^{4-}$ with a distorted cubane Ce_4Cl_4 core,[41] charge-balanced by Li^+ cations (see Figure 3). Rietveld refinement of the PND data measured at −248 °C reveal a η^3−BD_3−Ce coordination mode. The angles ∠Cl−Ce−Cl and ∠B−Ce−B are 73.26(16)° and 99.2(6)°, respectively, and the Ce−Cl and Ce−B distances are 2.961(6) and 2.74(2) Å, respectively. From the initial SR-PXD structural analysis some ambiguity existed concerning the position of the Li^+ ions and several structural models were investigated by Rietveld refinement of SR-PXD data and PND data and by DFT optimization, revealing that Li^+ ions are disordered, occupying 2/3 of the 12*d* Wyckoff site. Li^+ ions coordinate tetrahedrally four BD_4^- groups via the tetrahedral edge, i.e., η^2−BD_2−Li (Figure 3). Three B−D distances are determined to be 1.181(8) Å (D1), 1.22(1) Å (D2) and 1.231(7) Å (D3). The closest D···D contact is 1.9302(82) Å (D1−D3).

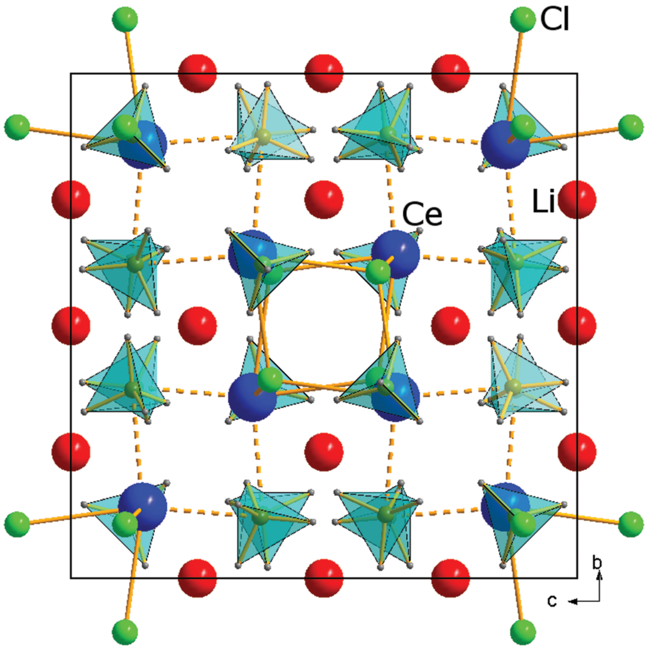

Figure 2. Crystal structure of the novel compound $LiCe(BH_4)_3Cl$. The BH_4 groups are shown as light blue tetrahedra and Ce−B coordinations are shown as broken bonds. The Li atoms are disordered over 12*d* Wyckoff site with an occupation of 2/3. On the figure the Li occupation is 1 for clarity.

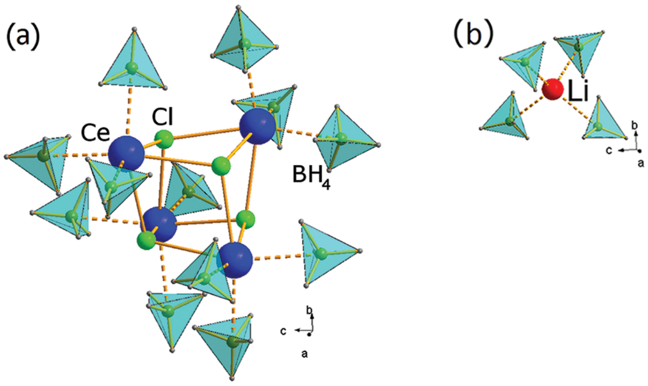

Figure 3. Isolated tetranuclear anionic clusters $[Ce_4Cl_4(BH_4)_{12}]^{4-}$ with (a) a distorted cubane Ce_4Cl_4 core and (b) tetrahedral Li coordination to four BH_4 groups.

As mentioned, a combined analysis of data from SR-PXD, PND and DFT optimization was utilized to locate the Li^+ ions. Besides the structure of $LiCe(BH_4)_3Cl$ described above with Li^+ positioned on the 12*d* Wyckoff site two other Li^+ positions were considered but eventually rejected (see Table 2). One of these two models corresponds to the only possible fully ordered arrangement of Li^+ ions on the sites 2*a* and 6*b*.[42] The 2*a* site is situated in the center of the distorted cubane cage Ce_4Cl_4, resulting in Ce−Li distance of only 2.8757(14) Å. For comparison, in a similar mixed metal borohydride chloride $NaY(BH_4)_2Cl_2$ the shortest Na−Y distance is 4.95 Å.[43] Indeed, DFT calculations on a model with the 2*a* site filled by Li^+ ions shows larger discrepancy for the position of Ce atoms with respect to the experimental data. Moreover, a Rietveld

Table 2. Overview of the Three Models for the Li Positions in Space Group $I\bar{4}3m$, Showing the Position and Idealized Occupancy of Li Sites

Li^+ Wyckoff site	PXD R_B[a](%)	PND R_B[a](%)	DFT eEnergy (eV/f.u.)[b]	idealized occupancy
12*d*	2.52	5.50	0	2/3
2*a*, 6*b*	3.38	6.96	0.42	1 (for both sites)
24*g*	2.51	5.19	1.14	1/3

[a] Not corrected for background. [b] Energy is calculated with respect to the lowest energy structure.

refinement of the occupancy for the 2*a* site gives a negative value of −0.8 using the SR-PXD data, questioning the credibility of the model.

In the third structural model for LiCe(BH$_4$)$_3$Cl, one-third of the 24*g* site (x = 0.12350, z = 0.57580) is occupied by Li$^+$ ions. However, DFT optimization showed large displacements of lithium and in particular hydrogen atom positions yielding a model inconsistent with neutron diffraction data. The Rietveld refinement using the SR-PXD data reveal unacceptably short Li−H distances of ∼1.2 Å. Because of the lack of agreement between the theoretical and experimental data the third model was also rejected.

DFT optimization showed that the 12*d* model (see Figure S1a in the Supporting Information) has the lowest energy and that the 2*a*/6*b* and the 24*g* model energies are higher by 0.42 and 1.14 eV/f.u, respectively. Furthermore, the optimized (center of the cage)−Ce distance for the 12*d* and 2*a* model are 2.905 and 3.114 Å, respectively. This difference makes a noticeable change in the simulated X-ray diffraction patterns since the heaviest atom Ce most strongly scatters X-rays and the 12*d* model reproduces the experimental pattern more closely (see the *R*-values in Table 2). DFT optimization reveals that relaxation of the unit cell volume leads to a rather large expansion of 11.1% while accompanying a small decrease in energy by 0.051 eV/f.u. for the model containing the 2*a* site. Contrary to that, the model with 12*d* site remains stable, with only 0.1% variation of the cell parameter and the related total energy changes of less than 1 meV/f.u. Another ordered variant of Li$^+$ configuration in the 12*d* site was modeled using DFT (see Figure S1 in the Supporting Information), which has higher energy by only 0.028 eV/f.u. and almost constant unit cell volume within 0.6% of the experimental value. The similarities in energy and volume between different hypothetically ordered 12*d* sites strongly support this model.

The formation energy for LiCe(BH$_4$)$_3$Cl from LiCl and Ce(BH$_4$)$_3$ has also been estimated using DFT calculations. Since the crystal structure of Ce(BH$_4$)$_3$ is unknown, the low temperature polymorph of Y(BH$_4$)$_3$ was adopted as a hypothetical "Ce(BH$_4$)$_3$" structure. Both LiCl and Ce(BH$_4$)$_3$ were simulated with the same approximations as LiCe(BH$_4$)$_3$Cl. The DFT optimized lattice parameter for "Ce(BH$_4$)$_3$" is a = 11.482 Å, which is somewhat larger than that of Y(BH$_4$)$_3$ (a = 10.852 Å) and rather close to that observed for LiCe(BH$_4$)$_3$Cl (a = 11.720 Å, this study), reflecting the relatively larger ionic radius of Ce and weaker binding as compared to Y(BH$_4$)$_3$. This may partly explain why formation of LiCe(BH$_4$)$_3$Cl is preferred to the formation of "Ce(BH$_4$)$_3$" under the same experimental condition. The reaction energy for (**2**) is estimated to be slightly endothermic.

$$\begin{aligned} \mathrm{LiCl} + \mathrm{Ce(BH_4)_3} &\rightarrow \mathrm{LiCe(BH_4)_3Cl}\ \Delta E \\ &= 13.9\ \mathrm{kJ/mol}\ (\text{or } 0.144\ \mathrm{eV}) \end{aligned} \tag{2}$$

Temperature effects are not taken into account and ΔE is the DFT total energy difference. Since the bonding characters are largely preserved between the reactants and the product, ΔH (T = 298 K) would not be significantly different from ΔE (T = 0 K). Therefore, the structure of LiCe(BH$_4$)$_3$Cl may be stabilized by higher entropy rather than lower enthalpy, and this result again favors the 12*d* model because disorder in Li positions would certainly contribute to the entropy.

In this study, a bimetallic borohydride chloride LiCe(BH$_4$)$_3$Cl is discovered, in contrast to other rare earth metal borohydrides produced mechano-chemically from similar metalborohydride-metalchloride reaction mixtures, i.e. LiSc(BH$_4$)$_4$,[15] Y(BH$_4$)$_3$,[44−48] and Gd(BH$_4$)$_3$,.[44,49] This dissimilarity might be due to differences in ionic ratio (given in parentheses) for the lanthanides as compared to lithium, i.e. Li$^+$ (0.76 Å) ≈ Sc^{3+} (0.75 Å) < Y^{3+} (0.90 Å) < Gd^{3+} (0.94 Å) < Ce^{3+} (1.02 Å). Apparently, anionic structures are preferred for the smallest ions, as in LiSc(BH$_4$)$_4$, and formation of monometallic framework structures seems to be more favorable for the slightly larger lanthanides, e.g., Y(BH$_4$)$_3$ and Gd(BH$_4$)$_3$. The largest lanthanides appear to facilitate formation of more complex framework structures, as for LiCe(BH$_4$)$_3$Cl, which contains isolated tetranuclear anionic clusters [Ce$_4$Cl$_4$(BH$_4$)$_{12}$]$^{4-}$ with a distorted cubane Ce$_4$Cl$_4$ core, charge-balanced by Li$^+$ cations.

Solid-State ^{11}B MAS NMR. The ^{11}B MAS NMR spectra of the central and satellite transitions for the deuterated sample CeCl$_3$−Li^{11}BD$_4$ (1:4, **s4**) recorded at 14.1 and 9.4 T (Figure 4) reveal manifolds of spinning side bands (ssb) from a single ^{11}B site, in agreement with the present crystal-structure determination. The appearance of the ssb manifolds in the three spectra is highly asymmetric and thereby deviates from the symmetric ssb patterns reported earlier for the ^{11}B central and satellite transitions in borohydride compounds.[19,47,50] Although asymmetries in the ssb intensities from the central and satellite transitions may arise from the combined effect of the ^{11}B quadrupole coupling and chemical shift anisotropy interactions, as demonstrated in ^{11}B MAS NMR spectra of borates,[51] the asymmetry in the present spectra reflects strong ^{11}B nuclear spin − paramagnetic electron-spin dipolar interactions[52,53] present along with the ^{11}B quadrupole coupling. Thus, the ^{11}B nuclear spin couples to the surrounding free electrons of the paramagnetic Ce^{3+} ions, in accordance with cerium present as the Ce^{3+} ion in LiCe(BH$_4$)$_3$Cl, i.e., the Ce^{4+} ion would result in a diamagnetic compound. In addition to the asymmetry of the ssb manifolds, these couplings also result in a significant line broadening of the individual ssbs. The fact, that the individual ^{11}B spins couple to the paramagnetic electron from several Ce^{3+} ions in different distances to the ^{11}B site and that these couplings are additive,[52] prevents a straightforward simulation of the ssb manifolds by consideration of the mutual effects from the ^{11}B quadrupole coupling and ^{11}B nuclear spin − paramagnetic electron-spin dipolar couplings. However, the observation of these heteronuclear dipolar couplings strongly suggests that the paramagnetic electron is localized in a Ce^{3+} bonding and that it is nonconducting. It is unlikely that the well-defined ^{11}B MAS NMR spectra shown in Figure 4 could have observed if the unpaired electrons were conducting. An estimation of the ^{11}B quadrupole coupling constant (C_Q) can

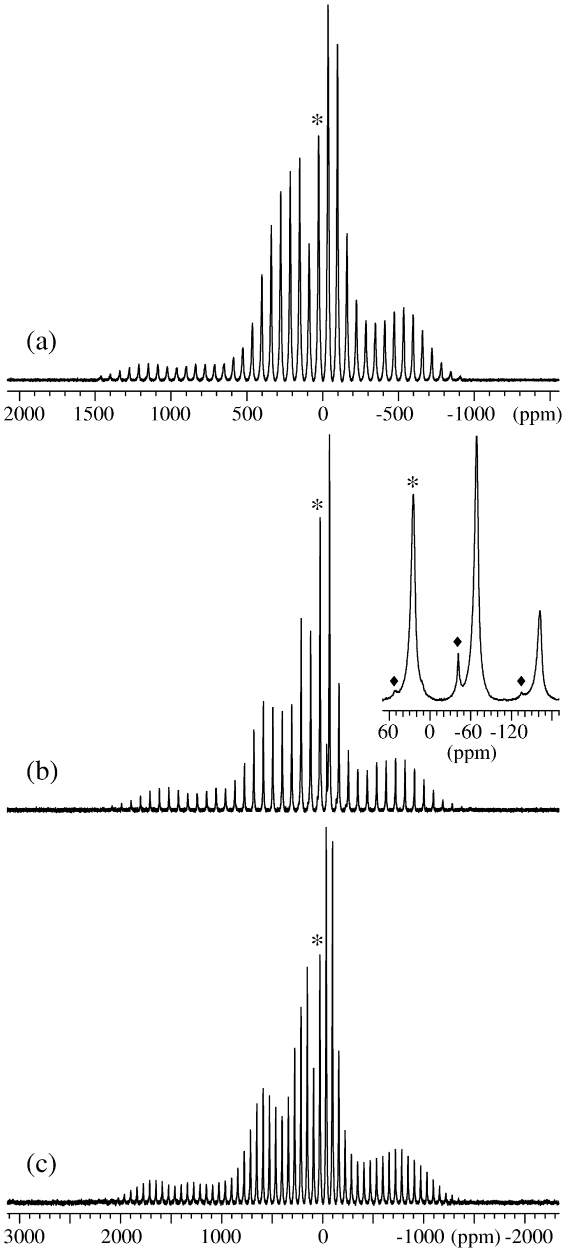

Figure 4. ^{11}B MAS NMR spectra of the central and satellite transitions for $CeCl_3$−$Li^{11}BD_4$ (1:3, s4) recorded at (a) 14.1 T and (b, c) 9.4 T, using spinning speeds of (a, b) ν_R = 12.0 kHz and (c) ν_R = 8.0 kHz. The spectra are shown with identical spectral widths in Hz. The asterisks indicate the isotropic peak. The inset in (b) illustrates the center band and first-order spinning sidebands (diamonds) from the small impurity of $LiBD_4$.

be achieved from the width of the ssb manifolds, which equals C_Q for a spin $I = 3/2$, assuming that the width is dominated by the first-order quadrupole interaction for the satellite transitions.[54] The ^{11}B MAS NMR spectra in Figure 4 are shown on identical widths in Hz, demonstrating that this is an acceptable approximation, and resulting in the estimated quadrupole coupling of C_Q = 420 kHz. This value is of the same magnitude as earlier reported ^{11}B quadrupole couplings for BH_4^- (BD_4^-) sites in borohydrides.[19,47,50] Moreover, apparent ^{11}B isotropic chemical shifts of δ_{iso} = 26.8 ppm and δ_{iso} = 26.1 ppm are determined[54] from the spectra recorded at 14.1 and 9.4 T (Figure 4a and b), respectively, assuming C_Q = 420 kHz and an axially symmetric quadrupole coupling tensor (η_Q = 0). Although these values are nearly identical, the apparent chemical shift for $LiCe(BD_4)_3Cl$ in **s4** is significantly shifted to high frequency as compared to the ^{11}B chemical shift range observed for BD_4^- sites in diamagnetic borohydrides (e.g., roughly from −35 to −47 ppm). This high-frequency shift may reflect that the ^{11}B spin − paramagnetic electron-spin interactions also contribute with a Knight shift of the ^{11}B resonance. ^{11}B MAS NMR spectra have also been acquired for the hydrogen samples, i.e. $LiCe(BH_4)_3Cl$ in **s1** − **s3** (not shown), which reveal the same centerband (δ = 26 ppm) and ssb manifold as observed for the deuterated sample (Figure 4) along with a centerband resonance at δ_{iso} = −41.2 ppm and a few associated ssbs from $LiBH_4$ in the samples. $LiBD_4$ is also observed in the **s4** sample, as most clearly seen in the 9.4 T spectrum recorded with a spinning speed of ν_R = 12.0 kHz (Figure 4b). However, evaluation of the intensities for the two compounds in this spectrum gives the intensity ratio $I(LiBD_4):I(LiCe(BH_4)_3Cl)$ = 0.03, demonstrating that the amount of $LiBD_4$ is very small in the **s4** sample.

Lithium Ion Conductivity. Conductivities are measured for $LiBH_4$ (Sigma-Aldrich, as received) and $LiCe(BH_4)_3Cl$ (sample $CeCl_3$−$LiBH_4$ 1:3, **s5**) pellets between steel disks acting as ionically blocking electrodes by impedance spectroscopy, at T = 20 °C. The impedance spectra recorded for $LiBH_4$ is shown in the Supporting Information, Figure S2. From the diameter of the semicircle observed at high frequency, which is related to the lithium ion mobility, a resistance of $R = 8.35 \times 10^5\ \Omega$ is measured for a 0.56 mm pellet thickness. This leads to a conductivity of 8.6×10^{-8} S cm^{-1} at 20 °C in good agreement with the values reported for orthorhombic *o*-$LiBH_4$.[55] No signature of the electrode interface or the grain boundaries are observed on the impedance spectra.

For $LiCe(BH_4)_3Cl$, impedance spectra were recorded on pellets of different thicknesses and Figure 5 reveal that the impedances are much lower than that of *o*-$LiBH_4$, in all cases. Only Warburg impedances related to the semi-infinite diffusion at the electrodes are observed and frequencies higher than 1 MHz are needed to fully plot the semicircles assigned to the lithium ion mobility in the material. Nevertheless, the shape of the impedance spectra is typical of a good conductor and the conductivity can be calculated from the intercept with the real axis (Z_{re} value). Figure 6 reveals for $LiCe(BH_4)_3Cl$ a linear relationship between the resistance and the pellet thickness.

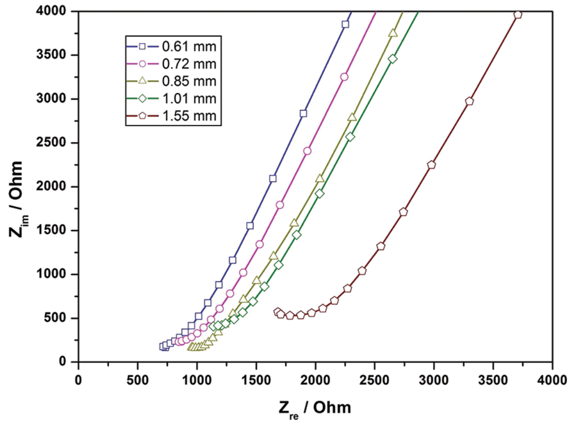

Figure 5. Complex impedance spectra for $CeCl_3$−$LiBH_4$ (1:3, s5) recorded on pellets of different thicknesses at T = 20 °C.

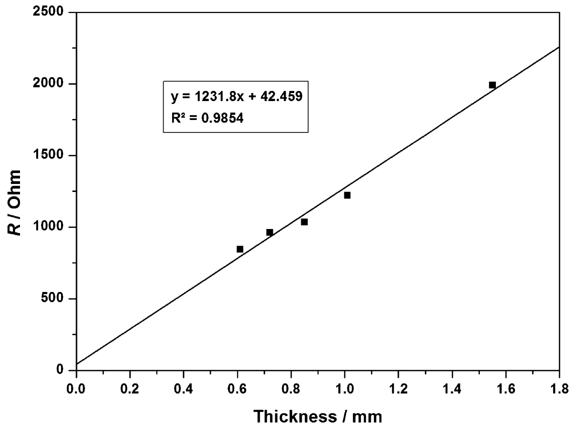

Figure 6. Resistance measured for the $CeCl_3$−$LiBH_4$ (1:3, s5) sample as a function of the pellet thickness (10 mm diameter). The extrapolated resistance for a 'zero thickness' is low (R_o = 42 Ω) showing the quality of the material-electrode interface. The slope of the linear fit is R = 1232 Ω mm^{-1}, which corresponds to a high conductivity of 1.03×10^{-4} S cm^{-1} measured at T = 20 °C.

The extrapolated resistance for a zero thickness is very low (R_o = 42 Ω) highlighting the quality of our electrode-material interface. The slope of the linear fit is R = 1232 Ω mm^{-1} hence for a 10 mm diameter pellet a conductivity of 1.03×10^{-4} S cm^{-1} is determined. The conductivity of the $LiCe(BH_4)_3Cl$ sample $CeCl_3$−$LiBH_4$ (1:3, **s5**) is therefore about 3 orders of magnitude higher than that of *o*-$LiBH_4$ at RT and is similar to that found for the hexagonal *h*-$LiBH_4$−LiI solid solution.[25,56,57]

Note that the $CeCl_3$−$LiBH_4$ (1:3, **s5**) sample is not a single phase: the sample composition determined by Rietveld refinement is $LiCe(BH_4)_3Cl$ 49 wt % (6 mol %), LiCl 17 wt % (84 mol %), and $CeCl_3$ 34 wt % (10 mol %). Nevertheless, as the conductivities of solid-state LiCl and $CeCl_3$ are very low at RT, the measured ionic conductivity undoubtedly originates from the $LiCe(BH_4)_3Cl$ compound. The volume fraction of $LiCe(BH_4)_3Cl$ in the $CeCl_3$−$LiBH_4$ (1:3, **s5**) sample is actually high (82%) and a percolation phenomenon occurs giving a high ionic conductivity to the pellet. Needless to say that a single-phase $LiCe(BH_4)_3Cl$ pellet should lead to higher conductivity values and that synthesis efforts are currently in progress in our laboratories.

To investigate more in detail the nature of the conduction, we also carried impedance spectroscopy out on a pellet sandwiched between lithium foils acting as ion nonblocking electrodes. On Figure 7, the resistivity is given for both the measurements made between steel disks and between lithium foils. The resistivity is similar in the case of the metallic lithium electrodes and the shape of the impedance curve resembles a curve for a good conductor. From the intercept with the real axis, a conductivity of 7×10^{-5} S cm^{-1} is obtained at 20 °C. This suggests that the $LiCe(BH_4)_3Cl$ sample $CeCl_3$−$LiBH_4$ (1:3, **s5**) is a good lithium ion conductor. The high lithium ion conductivity in $LiCe(BH_4)_3Cl$ may be attributed to empty Li positions in the structure. According to the structural model for $LiCe(BH_4)_3Cl$, only 2/3 of the Li positions (12*d* Wyckoff site) are occupied in a disordered manner. These first conductivity measurements suggest that $LiCe(BH_4)_3Cl$ could be considered as a future candidate for a solid electrolyte in the next-generation lithium-ion batteries. Recently, extremely high Li ion conductivity of 1.2×10^{-2} S cm^{-1} was reported for the novel compound $Li_{10}GeP_2S_{12}$.[58] ^{7}Li NMR experiments are in progress to demonstrate the high Li^+ mobility and to definitively conclude that the ionic conductivity originates solely from Li^+ cations.

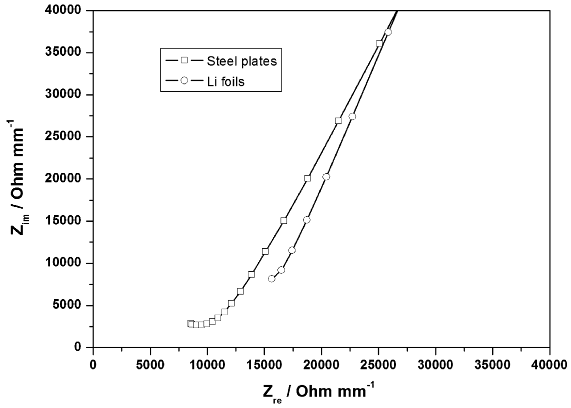

Figure 7. Complex impedance spectra for $CeCl_3$−$LiBH_4$ (1:3, s5) recorded with steel and Li metal electrodes at T = 20 °C.

Thermal Analysis and Sievert Measurements. Thermogravimetric (TGA) and differential scanning calorimetric (DSC) measurements for samples $CeCl_3$−$LiBH_4$ (1:3, **s2**) and (1:4, **s3**) are shown in Supporting Information, Figure S3, and Figure 8, respectively. Sample **s3** show a mass loss of 0.7 wt % in the temperature range 150 to 240 °C and a larger loss in the range 240 to 290 °C of 3.0 wt %. Thus, the observed mass loss for sample **s3** is 3.7 wt % in the temperature range RT to 500 °C, which is less than the calculated hydrogen content of the sample, 4.84 wt % H_2. The observed and calculated mass losses for sample **s2** are 3.2 and 3.88 wt % H_2, respectively. Considering that the decomposed samples contain cerium dihydride, CeH_2, the calculated hydrogen contents of the samples **s2** and **s3** are 3.23 and 4.23 wt % H_2.

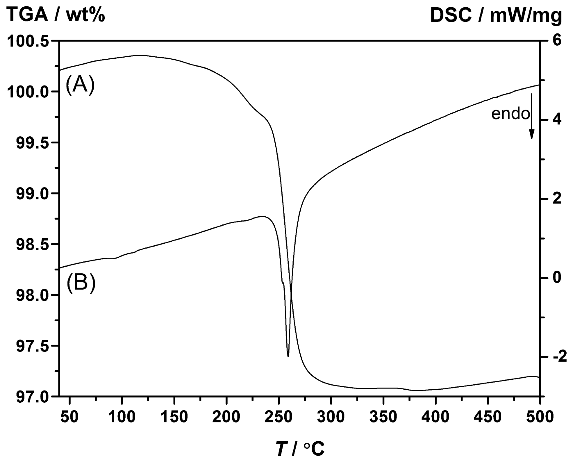

Figure 8. Thermal analysis,(A) TG and (B) DSC, data for $CeCl_3$−$LiBH_4$ (1:4, s3) measured in the temperature range RT to 500 °C (heating rate $\Delta T/\Delta t$ = 10 °C/min in He flow).

The DSC data for **s3** (see Figure 8) show two small endothermic peaks at 93 and 109 °C, which may correspond to the onset temperature for the reaction between remaining $CeCl_3$ and $LiBH_4$ in the sample (see reaction scheme 1) and to the polymorphic phase transition from orthorhombic to hexagonal $LiBH_4$. An endothermic peak observed at 213 °C may correspond to the melting of $LiCe(BH_4)_3Cl$. A smaller endothermic event observed at 240 °C may be associated with the initial decomposition of $LiCe(BH_4)_3Cl$. Indeed, the decomposition may consist of multiple reactions visible as shoulders at 257 and 261 °C at the major DSC signal with peak value at 266 °C. The endothermic events at 213 and 266 °C are correlated with the mass loss observed in the TGA data.

Reversible hydrogen storage properties were investigated using Sieverts measurements for sample **s3** and **s2** and the data is shown in Figure 9 and the Supporting Information, Figure S4, respectively. Desorption data for sample **s3** is collected in the Supporting Information, Table S3. Sample **s3** releases 0.5 wt % H_2 from RT to 220 °C and a major H_2 release of 3.25 wt % H_2 is observed from 220 to 270 °C, which corresponds to the observations by TGA and DSC. Additionally, 0.80 wt % H_2 is released during heating from 270 to 500 °C and 0.15 wt % H_2 is released after heating the samples for 3 h at a constant temperature of 500 °C. Hence, the total observed H_2 release is 4.7 wt % H_2 for sample **s3**. In a previous study of the $CeCl_3$–$LiBH_4$ system gas analysis revealed a very small amount of diboran during hydrogen desorption.[59] In the present study, the mass loss from the samples are all below the theoretical content of hydrogen; for this reason, the release of diboran from the samples is assumed to be at a minimum.

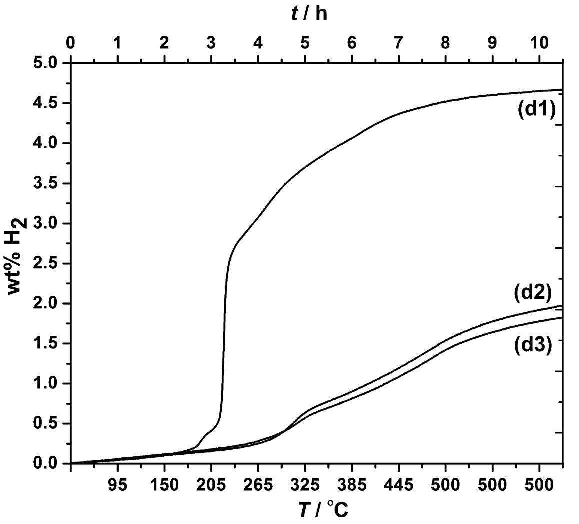

Figure 9. Sieverts type (PCT) measurement of the gas release from $CeCl_3$–$LiBH_4$ (1:4, s3), showing the first three desorptions, d1, d2, and d3, conducted in the temperature range RT to 500 °C (heating rate $\Delta T/\Delta t$ = 1 °C/min and with a back-pressure of $p(H_2)$ = 1 bar). Prior to d2 and d3, the sample was rehydrogenated at 400 °C and $p(H_2)$ = 100 bar for 24 h.

The Sieverts measurements for the second (d2) and third (d3) desorption follow a different trend since only 0.25 wt % H_2 is released in the temperature range RT to 270 °C. In contrast, desorptions d2 and d3 release 1.25 and 1.15 wt % H_2 from 270 to 500 °C and 0.5 and 0.4 wt % H_2 during 3 h at a constant temperature of 500 °C. Thus, the desorption d2 and d3 does not show the expected hydrogen release in the temperature range RT to 270 °C for the decomposition of $LiCe(BH_4)_3Cl$ revealing that the sample is not fully rehydrogenated at the selected conditions for hydrogen absorption. In total, the desorption d2 and d3 release 2.0 and 1.8 wt % H_2, which is slightly higher than the calculated hydrogen content assuming that CeH_2 or CeH_3 is formed during absorption of sample **s3**, i.e., 0.60 or 0.91 wt % H_2, respectively. The sample **s3** contain one equivalent excess $LiBH_4$, which may be rehydrogenated and the calculated hydrogen release from a sample **s3** containing CeH_2 and 1 equiv. of $LiBH_4$ is 2.12 wt % H_2. In contrast, sample **s2** release 3.75 wt % H_2 in the first cycle (d1) and 1.25 and 1.25 wt % H_2 in the second and third cycles, which is comparable to the calculated H_2 release of 3.88 and 0.97 wt % H_2 assuming that **s2** contain $LiCe(BH_4)_3Cl$ prior to d1 and CeH_3 for the later desorption cycles (see the Supporting Information, Figure S4). The decomposition products for **s3** after the third desorption (d3) in the Sieverts measurements (Figure 9) was investigated by Rietveld refinement of SR-PXD data (Figure 10). Diffraction from the decomposition products LiCl, CeH_2, and CeB_6 are identified along with an unknown compound.

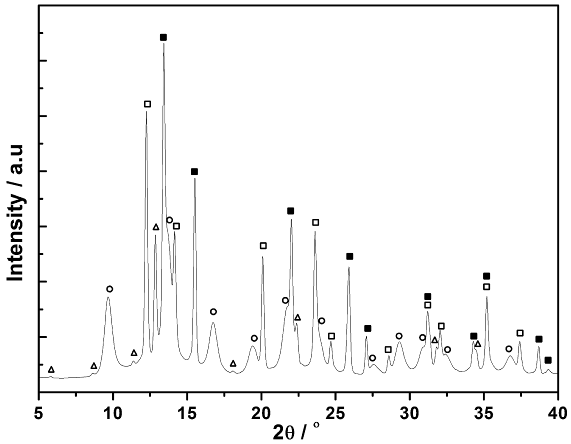

Figure 10. SR-PXD pattern of sample $CeCl_3$–$LiBH_4$ (1:4, s3) after the third desorption (d3) in the Sieverts measurements (Figure 8). The decomposition products CeB_6, LiCl, CeH_2 were identified by Rietveld refinement along with weak diffraction peaks from an unknown compound (ESRF, λ = 0.696713 Å, measured at RT). Symbols: ■ LiCl, □ CeH_2, ○ CeB_6, and Δ unknown.

Decomposition Mechanism for $LiCe(BH_4)_3Cl$ Observed by In situ SR-PXD. The thermal decomposition of samples $CeCl_3$–$LiBH_4$ (1:3, **s3**) and (1:4, **s4**) were studied by in situ SR-PXD. Both samples display similar decomposition mechanism, though the decomposition products from **s2** appear more crystalline and are discussed in the following (Figure 11). The first SR-PXD patterns in the series measured at RT show diffraction peaks from $LiCe(BH_4)_3Cl$, $CeCl_3$ and LiCl. The diffraction peaks from $CeCl_3$ decreases slowly at T > 63 °C and disappear at 315 °C. During heating from 100 to 160 °C the amounts of $LiCe(BH_4)_3Cl$ and LiCl increase, while that of $CeCl_3$ decreases because of the progress of reaction 1. The Bragg diffraction peaks from $LiCe(BH_4)_3Cl$ disappears at 240 °C, possibly because of melting and subsequent decomposition and diffraction from an unknown compound appear at 240 °C. Peaks from CeH_2 emerge at 320 °C when $CeCl_3$ disappears. The unknown compound may be a ternary salt composed of lithium, cerium and chloride and remains in the sample during the rest of the heating. A ternary salt, $NaYCl_4$, is also observed during the decomposition of $NaY(BH_4)_2Cl_2$.[43] Structural determination of the unknown compound has unfortunately not been possible, but further studies are currently being performed to elucidate the atomic composition. The reaction scheme (3) describes the idealized overall decomposition reaction for **s2** omitting the unknown compound.

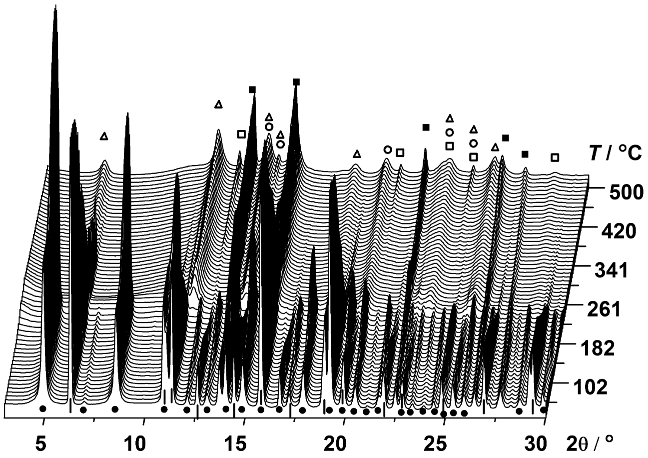

Figure 11. In situ SR-PXD data for $CeCl_3$–$LiBH_4$ (1:3, s2) measured from RT to 500 °C ($\Delta T/\Delta t$ = 8 °C/min, $p(Ar)$ = 1 bar, λ = 0.709637 Å). Symbols: ● $LiCe(BH_4)_3Cl$, | $CeCl_3$, ■ LiCl, □ CeH_2, ○ CeB_6, and Δ unknown.

$$LiCe(BH_4)_3Cl + 2LiCl \rightarrow 1/2CeH_2 + 1/2CeB_6 + 11/2H_2 + 3LiCl \quad (3)$$

CONCLUSION

The novel compound $LiCe(BH_4)_3Cl$ crystallizes in the cubic crystal system with the space group $I\bar{4}3m$ and the structure contains isolated tetranuclear anionic clusters $[Ce_4Cl_4(BH_4)_{12}]^{4-}$ with a distorted cubane Ce_4Cl_4 core charge-balanced by Li^+ cations. The Li^+ ions are disordered and occupy 2/3 of the 12*d* Wyckoff sites. The structural model was derived by the combined use of synchrotron radiation powder X-ray diffraction (SR-PXD), powder neutron diffraction (PND), and density functional theory (DFT) and would likely not have been obtained with any combination of only two of the methods. DFT indicates that $LiCe(BH_4)_3Cl$ is stabilized by higher entropy rather than lower enthalpy, in accord with the disorder at the Li positions. The structural model and DFT calculations agree well with the very high lithium ion conductivity measured for the $LiCe(BH_4)_3Cl$ containing sample, 1.03×10^{-4} S cm^{-1} at T = 20 °C. Conductivity measurements carried out between lithium foils suggest that the conductivity mainly originates from the high lithium ion mobility, which is in favor of our model of disordered Li. Solid-state ^{11}B MAS NMR spectra of the central and satellite transitions reveal that the ^{11}B spin interacts with the paramagnetic electron-spins (from the unpaired electron on Ce^{3+}), which also contribute with a Knight shift of the ^{11}B resonance. Very high lithium ion conductivity is in favor of our structural model including disordered Li. The new compound $LiCe(BH_4)_3Cl$ also stores 5.33 wt % hydrogen, which is released in the temperature range 220–260 °C. Rehydrogenation at moderate conditions leads to a reversible storage capacity of only ~1 wt % H_2.

ASSOCIATED CONTENT

Ⓢ Supporting Information

Additional tables and figures (PDF) and CIF. This material is available free of charge via the Internet at http://pubs.acs.org.

AUTHOR INFORMATION

Corresponding Author

*E-mail: yaroslav.filinchuk@uclouvain.be; trj@chem.au.dk. Tel: +45 8942 3894. Fax: +45 8619 6199.

Present Address

$^{\nabla}$Postdoctoral affiliate, Department of Material Science and Engineering, Massachusetts Institute of Technology, 77 Massachusetts Avenue, Cambridge, 02139, Massachusettes

Notes

The authors declare no competing financial interest.

ACKNOWLEDGMENTS

Dr. Denis Sheptyakov, Paul Scherrer Institut, PSI, Switzerland, is thanked for the powder neutron diffraction measurements and SNBL for beamtime allocation. We thank the Danish Natural Science Research Councils for fundings to the Instrument Centre for Solid-State NMR Spectroscopy and the research program DanScatt. The Danish Strategical Research Council is acknowledged for financial support to the Center for Energy Materials (CEM) and The Danish National Research Foundation for fundings to the Center for Materials Crystallography (CMC). Y.-S.L. and Y.W.C. acknowledge support by the Hydrogen Energy R&D Center, funded by the Ministry of Education, Science and Technology of Korea.

REFERENCES

(1) MacKay, D. J. C. *Sustainable Energy — without the Hot Air*; UIT: Cambridge, 2009.

(2) Fichtner, M. *J. Alloys Compd.* **2011**, *509*, S529–S534.

(3) Eberle, U.; Felderhoff, M.; Schüth, F. *Angew. Chem., Int. Ed.* **2009**, *48*, 6608–6630.

(4) Goodenough, J. B.; Kim, Y. *Chem. Mater.* **2009**, *22*, 587–603.

(5) Li, H. W.; Yan, Y.; Orimo, S.; Züttel, A.; Jensen, C. M. *Energies* **2011**, *4*, 185–214.

(6) Orimo, S.-ichi; Nakamori, Y.; Eliseo, J. R.; Züttel, A.; Jensen, C. M. *Chem. Rev.* **2007**, *107*, 4111–4132.

(7) Grochala, W.; Edwards, P. P. *Chem. Rev.* **2004**, *104*, 1283–1316.

(8) Ravnsbæk, D. B.; Filinchuk, Y.; Cernỳ, R.; Jensen, T. R. *Z. Kristallogr.* **2010**, *225*, 557–569.

(9) Rude, L. H.; Nielsen, T. K.; Ravnsbæk, D. B.; Bösenberg, U.; Ley, M. B.; Richter, B.; Arnbjerg, L. M.; Dornheim, M.; Filinchuk, Y.; Besenbacher, F.; Jensen, T. R. *Phys. Stat. Solidi (A)* **2011**, *208*, 1754–1773.

(10) Nakamori, Y.; Li, H.-W.; Kikuchi, K.; Aoki, M.; Miwa, K.; Towata, S.; Orimo, S. *J. Alloys Compd.* **2007**, *446–447*, 296–300.

(11) Züttel, A.; Borgschulte, A.; Orimo, S. I. *Scr. Mater.* **2007**, *56*, 823–828.

(12) Ravnsbæk, D. B.; Sørensen, L. H.; Filinchuk, Y.; Besenbacher, F.; Jensen, T. R. *Angew. Chem., Int. Ed.* **2012**, *51*, 3582–3586.

(13) Filinchuk, Y.; Richter, B.; Jensen, T. R.; Dmitriev, V.; Chernyshov, D.; Hagemann, H. *Angew. Chem., Int. Ed.* **2011**, *47*, 11162–11166.

(14) Ravnsbæk, D. B.; Filinchuk, Y.; Cerenius, Y.; Jakobsen, H. J.; Besenbacher, F.; Skibsted, J.; Jensen, T. R. *Angew. Chem., Int. Ed.* **2009**, *48*, 6659–6663.

(15) Černý, R.; Chul Kim, K.; Penin, N.; D'Anna, V.; Hagemann, H.; Sholl, D. S. *J. Phys. Chem. C* **2010**, *114*, 19127–19133.

(16) Hagemann, H.; Longhini, M.; Kaminski, J. W.; Wesolowski, T. A.; Černý, R.; Penin, N.; Sørby, M. H.; Hauback, B. C.; Severa, G.; Jensen, C. M. *J. Phys. Chem. A* **2008**, *112*, 7551–7555.

(17) Kim, C.; Hwang, S.-J.; Bowman, R. C.; Reiter, J. W.; Zan, J. A.; Kulleck, J. G.; Kabbour, H.; Majzoub, E. H.; Ozolins, V. *J. Phys. Chem. C* **2009**, *113*, 9956–9968.

(18) Černý, R.; Severa, G.; Ravnsbæk, D. B.; Filinchuk, Y.; d' Anna, V.; Hagemann, H.; Haase, D.; Jensen, C. M.; Jensen, T. R. *J. Phys. Chem. C* **2010**, *114*, 1357−1364.

(19) Černý, R.; Ravnsbæk, D. B.; Severa, G.; Filinchuk, Y.; D' Anna, V.; Hagemann, H.; Haase, D.; Skibsted, J.; Jensen, C. M.; Jensen, T. R. *J. Phys. Chem. C* **2010**, *114*, 19540−19549.

(20) Ravnsbæk, D. B.; Sørensen, L. H.; Filinchuk, Y.; Reed, D.; Book, D.; Jakobsen, H. J.; Besenbacher, F.; Skibsted, J.; Jensen, T. R. *Eur. J. Inorg. Chem.* **2010**, *11*, 1608−1612.

(21) Züttel, A.; Rentsch, S.; Fischer, P.; Wenger, P.; Sudan, P.; Mauron, P.; Emmenegger, C. *J. Alloys Compd.* **2003**, *356*−*357*, 515−520.

(22) Mosegaard, L.; Møller, B.; Jørgensen, J.-E.; Filinchuk, Y.; Cerenius, Y.; Hanson, J. C.; Dimasi, E.; Besenbacher, F.; Jensen, T. R. *J. Phys. Chem. C* **2008**, *112*, 1299−1303.

(23) Arnbjerg, L. M.; Ravnsbæk, D. B.; Filinchuk, Y.; Vang, R. T.; Cerenius, Y.; Besenbacher, F.; Jørgensen, J. E.; Jakobsen, H. J.; Jensen, T. R. *Chem. Mater.* **2009**, *21*, 5772−5782.

(24) Rude, L. H.; Groppo, E.; Arnbjerg, L. M.; Ravnsbæk, D. B.; Malmkjær, R. A.; Filinchuk, Y.; Baricco, M.; Besenbacher, F.; Jensen, T. R. *J. Alloys Compd.* **2011**, *509*, 8299−8305.

(25) Maekawa, H.; Matsuo, M.; Takamura, H.; Ando, M.; Noda, Y.; Karahashi, T.; Orimo, S.-ichi *J. Am. Chem. Soc.* **2009**, *131*, 894−895.

(26) Tarascon, J. M.; Armand, M. *Nature* **2001**, *414*, 359−367.

(27) Kostka, J.; Lohstroh, W.; Fichtner, M.; Hahn, H. *J. Phys. Chem. C* **2007**, *111*, 14026−14029.

(28) Hammersley, A. P.; Svensson, S. O.; Hanfland, M.; Fitch, A. N.; Hausermann, D. *High Pressure Res* **1996**, *14*, 235−248.

(29) Vogel, S.; Ehm, L.; Knorr, K.; Braun, C. *Adv. X-ray Anal.* **2002**, *45*, 31−33.

(30) Fischer, P.; Frey, G.; Koch, M.; Könnecke, M.; Pomjakushin, V.; Schefer, J.; Thut, R.; Schlumpf, N.; Bürge, R.; Greuter, U. *Phys. B: Condens. Matter* **2000**, *276*, 146−147.

(31) Boultif, A.; Louër, D. *J. Appl. Crystallogr.* **2004**, *37*, 724−731.

(32) Favre-Nicolin, V.; Cerný, R. *J. Appl. Crystallogr.* **2002**, *35*, 734−743.

(33) Spek, A. *Acta Crystallogr., Sect A* **1990**, *46*, c34.

(34) Rodriguez-Carvajal, J. *FULLPROF SUITE*; Laboratoire Leon Brillouin and Laboratory of Solid State Chemistry and Inorganic Molecular Chemistry: Saclay and Rennes, France, 2003.

(35) Perdew, J. P.; Burke, K.; Ernzerhof, M. *Phys. Rev. Lett.* **1997**, *78*, 3865.

(36) Kresse, G.; Furthmüller, J. *Phys. Rev. B* **1996**, *54*, 11169.

(37) Blöchl, P. E. *Phys. Rev. B* **1994**, *50*, 17953.

(38) Bestpractices H2 Storage Materials www1.eere.energy.gov/hydrogenandfuelcells/pdfs/ bestpractices_ h2_storage_materials.pdf.

(39) PCTPro-2000 - Calorimetry and thermal analysis http://www.setaram.com/PCTPro-2000.htm (accessed Jan 21, 2010).

(40) Gennari, F. C.; Esquivel, M. R. *J. Alloys Compd.* **2009**, *485*, L47−L51.

(41) Mak, T. C. W.; Mok, F. C. *J. Chem. Crystallogr.* **1978**, *8*, 183−191.

(42) Frommen, C.; Sørby, M. H.; Ravindran, P.; Vajeeston, P.; Fjellvåg, H.; Hauback, B. C. *J. Phys. Chem. C* **2011**, *115* (47), 23591−23602.

(43) Ravnsbæk, D. B.; Ley, M. B.; Lee, Y.-S.; Hagemann, H.; d' Anna, V.; Cho, Y. W.; Filinchuk, Y.; Jensen, T. R. *Int. J. Hydrogen Energy* **2012**, DOI: 10.1016/j.ijhydene.2012.02.130.

(44) Sato, T.; Miwa, K.; Nakamori, Y.; Ohoyama, K.; Li, H.-W.; Noritake, T.; Aoki, M.; Towata, S.-ichi; Orimo, S.-ichi *Phys. Rev. B* **2008**, *77*, 104114.

(45) Lee, Y.-S.; Shim, J.; Cho, Y. *J. Phys. Chem. C.* **2010**, *114*, 12833−12837.

(46) Jaroń, T.; Grochala, W. *Dalton Trans.* **2010**, *39*, 160−166.

(47) Ravnsbæk, D. B.; Filinchuk, Y.; Černý, R.; Ley, M. B.; Haase, D.; Jakobsen, H. J.; Skibsted, J.; Jensen, T. R. *Inorg. Chem.* **2010**, *49*, 3801−3809.

(48) Frommen, C.; Aliouane, N.; Deledda, S.; Fonneløp, J. E.; Grove, H.; Lieutenant, K.; Llamas-Jansa, I.; Sartori, S.; Sørby, M. H.; Hauback, B. C. *J. Alloys Compd.* **2010**, *496*, 710−716.

(49) Andrade-Gamboa, J.; Puszkiel, J. A.; Fernández-Albanesi, L.; Gennari, F. C. *Int. J. Hydrogen Energy* **2010**, *35*, 10324−10328.

(50) Ravnsbæk, D. B.; Frommen, C.; Reed, D.; Filinchuk, Y.; Sørby, M. H.; Hauback, B. C.; Jakobsen, H. J.; Book, D.; Besenbacher, F.; Skibsted, J.; Jensen, T. R. *J. Alloys Compd.* **2011**, *509*, 698−704.

(51) Hansen, M. R.; Vosegaard, T.; Jakobsen, H. J.; Skibsted, J. *J. Phys. Chem. A* **2004**, *108*, 586−594.

(52) Nayeem, A.; Yesinowski, J. P. *J. Chem. Phys.* **1988**, *89*, 4600−4608.

(53) Grey, C. P.; Dupre, N. *Chem. Rev.* **2004**, *104*, 4493−4512.

(54) Skibsted, J.; Nielsen, N. C.; Bildsøe, H.; Jakobsen, H. J. *J. Magn. Reson.* **1991**, *95*, 88−117.

(55) Matsuo, M.; Nakamori, Y.; Orimo, S.; Maekawa, H.; Takamura, H. *Appl. Phys. Lett.* **2007**, *91*, 224103.

(56) Matsuo, M.; Takamura, H.; Maekawa, H.; Li, H.-W.; Orimo, S.-i. *Appl. Phys. Lett.* **2009**, *94*, 084103.

(57) Miyazaki, R.; Karahashi, T.; Kumatani, N.; Noda, Y.; Ando, M.; Takamura, H.; Matsuo, M.; Orimo, S.; Maekawa, H. *Solid State Ionics* **2010**, *192*, 143−147.

(58) Kamaya, N.; Homma, K.; Yamakawa, Y.; Hirayama, M.; Kanno, R.; Yonemura, M.; Kamiyama, T.; Kato, Y.; Hama, S.; Kawamoto, K. *Nat. Mater.* **2011**, *10*, 682−686.

(59) Zhang, B. J.; Liu, B. H.; Li, Z. P. *J. Alloys Compd.* **2011**, *509*, 751−757.